Cellulose (2021) 28:9207–9226
https://doi.org/10.1007/s10570-021-04072-6

ORIGINAL RESEARCH

Antibacterial nano-biocomposite scaffolds of Chitosan, Carboxymethyl Cellulose and Zn & Fe integrated Hydroxyapatite (Chitosan-CMC-FZO@HAp) for bone tissue engineering

Varun Saxena · Abshar Hasan · Lalit M. Pandey

Received: 23 March 2021 / Accepted: 7 July 2021 / Published online: 26 July 2021

Abstract The polymeric scaffolds are one of the most studied systems for biomedical applications. Yet, their enzymatic degradation and non-antibacterial ability are the major challenges for the researchers. In this regard, we designed Fe(III) doped ZnO integrated hydroxyapatite ZFHAp nanoparticles and prepared the natural biopolymer-based chitosan- carboxymethyl cellulose-ZFHAp scaffolds suitable for bone tissue engineering. The nanoparticles were successfully characterized with XRD and RAMAN spectroscopy and were found to be in hexagonal wurtzite HAp phase with Ca + Zn + Fe/P ratio of 1.7. The prepared nano-biocomposite scaffolds were microporous in structure (25–123 µm), and their biochemical behaviours such as porosity (60–80%), swelling, and enzymatic degradation (21–50%) were dependent on the concentrations of ZFHAp. The swelling and degradation of the prepared scaffolds were linearly related. The presence of 5% ZFHAp in the scaffolds (SCA-5) resulted in pore size of 92 ± 10 µm and 50% degradation time of 42 days. This scaffolds SCA-5 also showed self-antibacterial activities along with excellent cell proliferation ability. The present study designates the SCA-5 as plausible scaffolds for bone tissue engineering.

Keywords Chitosan · Carboxymethyl cellulose · Nano-hydroxyapatite · Nano-biocomposite scaffold · Degradation · Porosity · Cell proliferation · Self-antibacterial activity

Supplementary Information The online version contains supplementary material available at https://doi.org/10.1007/s10570-021-04072-6.

V. Saxena · A. Hasan · L. M. Pandey (✉)
Department of Biosciences and Bioengineering, Bio-Interface & Environmental Engineering Lab, Indian Institute of Technology Guwahati, Guwahati, Assam 781039, India
e-mail: lalitpandey@iitg.ac.in

Introduction

For the appropriate cell attachment and proliferation, 3D scaffolds are the most studied systems in bone tissue engineering. The major benefits of using scaffolds include the high specific surface area, porous structure, and ability to adhere to a large number of cells (Hasan et al. 2018b). Different natural and synthetic polymers have been tested for creating antimicrobial surfaces (Hasan et al. 2020a, b), 3D scaffolds/constructs for various biomedical applications, such as bone tissue engineering (Atila et al. 2019; Wang et al. 2018) and tissue regeneration (Atila et al. 2019). Among all the naturally occurring polymers, chitosan is one of the most studied polymers for bone tissue engineering applications (Gámiz González et al. 2017; Maitra 2005; Saxena et al. 2019). Chitosan possesses many properties desired for

biomedical applications like biodegradability, biocompatibility, bioactivity, and antimicrobial properties (Hasan et al. 2018b). However, the presence of β-1,4 glycosidic linkage makes it more prone to degradation by lysozyme and other body fluids (Benbow et al. 2020), restricting its applicability for the controlled cell growth, antibacterial action and biomolecule delivery. Hence, nanocomposite scaffolds were scrutinized to remove these lags.

Crosslinking within polymers has proven to guard the hydrophilicity and water solubility (Schoolaert et al. 2020). Carboxymethylcellulose (CMC), an anionic polymer with chemical similarity with chitosan, provides a strong ionic crosslinking due to short distance between short distances between H4 and H1′ across the glycosidic linkage (French and Johnson 2009) to enhance the biochemical feature, *i.e.* swelling, porosity, and degradation (Sun et al. 2018). Cellulose has also been utilized for various biomedical applications (Ling et al. 2019; Wahlström et al. 2020; Wallecan and Debon 2018; Zhao et al. 2020). Further, chitosan, CMC, and their composites have been integrated with various inorganic materials such as hydroxyapatite (HAp), to achieve the desired mechanical strength along with biochemical behavior. The swelling and degradation behaviors remain directly dependent on the porous nature of the scaffolds. Hence, the most suitable way to control biochemical behavior is to control the porosity. Yet the tunability of these behaviors is still under extensive research due to interconnections between porosity, composition, mechanical properties, and bioactivity. The challenge remains to control the biochemical features without compromising the mechanical properties, *i.e.* strength and biological behavior (bioactivity) and vice-versa. Hence, various approaches have been devised to design nano-sized HAp, its integration with chitosan and/or CMC for bone tissue engineering (Guerzoni et al. 2014; Kharaghani et al. 2020). These scaffolds have been found to possess decent mechanical strength comparable to that of callous bone, *i.e.* 2–10 MPa (Baskaran et al. 2017; Miyaji et al. 2005; Saxena et al. 2018b; Šupová 2015).

With the recent advancements, it was realized that these systems lack inherent antibacterial activity. Various nanoparticles of Ag, Cu, and Zn with antibacterial properties have been studied to impart the self-antibacterial characteristics to polymers (Fontenot et al. 2019; Hasan et al. 2018b). Among them, ZnO nanoparticles are the most explored because of their cost-effectiveness (Samani et al. 2013). However, the higher minimum inhibitory concentration (MIC) and cytotoxicity due to the generation of reactive oxygen species (ROS) limit the practical applications. Recently, it was reported that doping of transition metals (Al, Fe) reduced the MIC concentrations and blocked the ROS generation (Awwad et al. 2020; Saxena et al. 2018a; Saxena and Pandey 2020; Srilakshmi and Saraf 2016; Xiu et al. 2012). Additionally, the integration of Fe (III) into ZnO caused the linear release of Zn^{2+} ions leading to the rupturing of the bacterial cell wall (Saxena and Pandey 2020). Hence the integration of Fe doped ZnO (FZO) with nano-HAp is expected to incorporate the desired antibacterial activity into the HAp matrix. The incorporation of antibacterial activity in the scaffolds without affecting their biochemical behavior remains another major bottleneck in designing the self-antibacterial systems.

In this study, we have synthesized chitosan-CMC and FZO integrated HAp (Chitosan-CMC-FZO@-HAp) based nanocomposite scaffolds to achieve the inherent antibacterial activity within the scaffold, as well as to control the porosity of the scaffold. Hence, the novelty of this work remains in incorporating self antibacterial activity into a HAp based scaffold without generating the secondary phases such as β-Tricalcium phosphate, and controlling the biochemical behavior. Henceforth, the present study will provide an insight into designing the polymeric scaffolds with self-antibacterial properties along with controlled biochemical behavior. The effects of various amounts of FZO@HAp on the biochemical properties (porosity, swelling, and degradation) and antibacterial activity have been investigated.

Experimental section

Materials

The precursors for the synthesis of ZFHAp nanoparticles such as calcium nitrate tetrahydrate $Ca(NO_3)_2.4H_2O$, (GRM496), diammonium hydrogen phosphate $(NH_4)_2.HPO_4$ (GRM1271), zinc nitrate hexahydrate, $Zn(NO_3)_2.6H_2O$ (GRM691), sodium hydroxide, NaOH (MB095) were purchased from Himedia, India. Ferric chloride anhydrous $FeCl_3$ (231–729-4) was

obtained from Merck India. These chemicals were used without any modification. For the scaffold synthesis, chitosan (CS, Mw = 50–190 kDa and degree of deacetylation = 75–85%, Cat No. 448869) was procured from Sigma, India, and CMC-sodium (RM10844; the degree of substitution of 0.9) was purchased from Himedia, India. Double distilled water (MiliQ, 18 mΩ, Millipore systems) was used throughout the experiments.

Synthesis of ZFHAp nanoparticles

In our previous studies, it was found that 15% doping of metal ions (Al and Fe) into ZnO improve its antibacterial activity (Saxena et al. 2018a; Saxena and Pandey 2020). Based on these results, the 15% integration was implied in this study to obtain composites that can exhibit higher antibacterial activity. Towards this, 0.85 M of Ca was added with 0.10 M of Zn and 0.05 M of Fe (III) to acquire the desired antibacterial activity. The ZFHAp nanoparticles were synthesized via a simple co-precipitation method (Saxena et al. 2018a). Briefly, 0.85 M $Ca(NO_3)_2.4H_2O$, 0.10 M $Zn(NO_3)_2.6H_2O$, and 0.05 M of Ferric chloride anhydrous $FeCl_3$ aqueous solution (50 ml) was titrated with 0.6 M $(NH_4)_2.HPO_4$ aqueous solution (50 ml) at 65 °C temperature. The final molar ratio was kept constant with Ca + Zn + Fe/P = 1.67. After the addition, the pH was enhanced to 11 by adding NH_4OH solution in a dropwise manner. After 3 h, the solution was kept for 24 h aging followed by several times washing with deionized until neutral pH. The samples were then air-dried at 80 °C in a hot air oven followed by sintering at 650 °C.

Preparation of chitosan-CMC-ZFHAp scaffold

The nanocomposite scaffold of Chitosan, CMC, and HAp/ZFHAp was prepared by mixing the chitosan and CMC at 2% (w/v) and varying the concentrations of HAp/ZFHAp (Hasan et al. 2018b). Briefly, 2% (w/v) chitosan solution in acetic acid was mixed with 2% (w/v) of CMC for 3 h. After proper mixing various concentrations of designed HAp/ZFHAp nanoparticles (0, 1%, 2%, 2.5%, 5%, 10% (w/v)) was mixed to the chitosan-CMC mixture until a homogenous mixture was achieved. The mixtures were frozen at −20 °C, and pH neutralized using 1 M NaOH prior to freeze-drying under vacuum. The prepared scaffolds were stored under vacuum for their characterization and applications. The scaffolds were named as listed in Table 1, and the same sample codes are referred throughout the manuscript.

Physical characterizations of ZFHAp nanoparticles

The biological properties of nanoparticles majorly depend on their shape and morphology (Saxena et al. 2018b). Hence, morphological analysis remains an important factor for biomaterial research. The phase analysis of the synthesized ZFHAp samples was done using an X-ray diffractometer (XRD, Rigaku, Ultima IV, Japan) equipped with Cu Kα radiation (λ = 1.5406 nm). A slow step size (2θ of 0.02°) was implied for the measurement. Raman spectroscopic analysis (LabRam HR laser micro Raman system, Horiba) of the ZFHAp samples was carried out at 532 nm wavelength of incident laser light. The shape and size of the ZFHAp samples were analyzed using Field emission scanning electron microscopy (FESEM, Zeiss, Sigma), and the elemental analysis was carried out by recording the EDAX data using the same FESEM instrument. ImageJ software was applied to analyze the images to calculate the particle size.

Biochemical characterizations and mechanical strength analysis of the scaffolds

After successfully analyzing the physical features, the scaffolds were scrutinized for their various biochemical analysis, as discussed below.

Porosity of scaffolds

The porosity of the scaffolds was evaluated using the liquid displacement method as studied previously (Sivashankari and Prabaharan 2020). In brief, the scaffolds were cut into pieces and the known weight of scaffolds (W_d) were immersed in hexane under vacuum for the forced entry of hexane into the microporous scaffolds. The scaffolds were quickly transferred into the pre-weighed weighing bottles containing known weight (W_1) and volume (V_1) of hexane and the final weight (W_2) and volume (V_2) were recorded. The porosity of the scaffolds was calculated using the following equation-1.

Table 1 Sample codes of scaffolds with various concentrations of ZFHAp

S.n	Sample code	Chitosan (w/v)%	CMC (w/v)%	ZFHAp (w/v)%	Hap (w/v)%
1	SCA-0	2	2	0	0
2	SCA-1	2	2	1	0
3	SCA-2	2	2	2	0
4	SCA-2.5	2	2	2.5	0
5	SCA-5	2	2	5	0
6	SCA-10	2	2	10	0
7	HSCA-2.5	2	2	0	2.5
8	HSCA-5	2	2	0	5
9	HSCA-10	2	2	0	10

$$\varnothing\% = \frac{W_2 - W_1 - W_d}{\rho(V_2 - V_1)} \quad (1)$$

where ρ is the density of hexane, *i.e.* (0.655 gcm^{-3}).

Swelling behavior of scaffolds

For various biomedical applications of the scaffold, along with porosity, the swelling behavior also plays a key role. The bioactivity of a scaffold is majorly dependent on its fluid retention, fluid transfer, and swelling behavior. Along with porosity, swelling behavior governs the degradation behavior of the scaffolds leading to its bone integration ability. To analyze the swelling behavior of the scaffolds, the known weight of scaffolds (W_i) were treated with the Phosphate Buffer Saline (PBS, pH-7.4) for various time intervals at 37 °C. At each time interval, the scaffolds were removed and dried using blotting paper. The dried weight (W_f) was measured, and the swelling behavior Q (%) was analyzed using the following equation-2.

$$\%Swelling(Q) = \frac{W_f - W_i}{W_i} \times 100 \quad (2)$$

The above Q_t data was fitted a second-order swelling kinetics model (Vilela et al. 2019) using as given in Eq. 3.

$$Q_t = \frac{k_s Q_e^2 t}{1 + k_s Q_e t} \quad (3)$$

where k_s is the 2nd order rate constant (g g^{-1} min^{-1}) swelling rate constant and Q_e represents the theoretical equilibrium swelling capacity (g g^{-1}).

Enzymatic degradation of scaffolds

The enzymatic degradation studies were carried out using the lysozyme (2 mg mL^{-1}) in PBS solution (pH-7.4). For this purpose, the known weight of scaffolds (M_i) were subjected to the lysozyme-PBS solution under constant stirring (60 rpm) at 37 °C for the different durations, *i.e.* 4, 8, 12, 16, and 20 days. The lysozyme-PBS solution was replaced regularly with a fresh solution. After the treatment, the scaffolds were freeze-dried, and the final weight of the scaffolds (M_f) were calculated. The degradation (%) was calculated using the following equation-4.

$$Degradation\% = \frac{M_f - M_i}{M_i} \times 100 \quad (4)$$

In addition, degradation kinetics was also studied. The degradation data were fitted using the first order equation-5 to estimate the degradation rate constant k_d(day^{-1}) and 50% scaffold degradation (T_{50}).

$$M_t = M_i(1 - e^{-k_d t}) \quad (5)$$

Mechanical strength analysis

The mechanical strength of scaffolds was determined using an Electromechanical Universal Testing Machine (UTM) instrument (Zwick Roell: Z005TN) equipped with a 5kN load cell with a crosshead speed of 1 mm/min.

Biological activity of scaffolds

After successful synthesis and biochemical characterizations of scaffolds, the prepared scaffolds were subjected to their biological investigations for

practical applications. For this purpose, the antibacterial activities as well as the cell proliferation analysis were performed.

Antibacterial activity

Many of the implanted biomaterials exhibit bacterial contamination due to surgical procedures, which lead to immunogenic responses and ultimately resulting in the rejection of the implants. Thus it is desirable to impart additional antibacterial characteristics in the biomaterials to prevent such unwanted processes and implant failure. The antibacterial activity was tested against two Gram-negative strains (*E. coli*, MTCC 1610 and *S. paratyphi*, MTCC 735) and two Gram-positive strains (*L. monocytogenes*, (ATCC 19,115) and *S. aureus*, MTCC 6538) using ASTM G 21–09 protocol, as reported previously (Hasan et al. 2018b). Briefly, scaffold discs of 15 mm diameter were first washed with 70% alcohol and MilliQ water to remove the adhered bacteria, if any, followed by rinsing with sterilized water. The bacterial culture (100 µL, 1.0×10^6 CFU mL^{-1}) was seeded on the SCA-0, SCA-2.5, SCA-5, HSCA-2.5, and HSCA-5 scaffolds, and were incubated at 37 °C for 24 h. After the incubation, the scaffolds were washed with 0.87 wt % NaCl solution containing 0.03 wt % Tween 80. The washed solution was diluted suitably and speared over a freshly prepared agar plate. The agar plates were incubated at 37 °C for 24 h. The scaffolds with excellent antibacterial activity (0% growth) were further investigated for bone cell proliferation.

Bone cell proliferation analysis

The successful synthesis of scaffolds is sustained by its efficiency for cell proliferation. The selective killing of bacterial cells and support to the human cells for their attachment and proliferation is the key for biomedical applications. The bone cell proliferation ability of the scaffolds was studied using MG-63 cell line procured from NCCS Pune India. The cells were first grown to their confluency in a T25 flask at 37 °C, 5% CO_2 and 85% humidity under a CO_2 incubator. Dulbecco's modified Eagle's medium (DMEM) supplemented with 10% fetal bovine serum (FBS, Invitrogen) and 1% antibiotic (Pen Strep, Invitrogen) was used for this experiment. The scaffold with no bacterial growth was analyzed for *in-vitro* cell proliferation. 1×10^5 cells mL^{-1} of MG-63 were seeded on the scaffolds for 5 days DMEM media and incubated at 37 °C and 5% CO_2. After 5 days, the scaffolds were washed with sterilized PBS (pH-7.4) multiple times for the removal of unadhered cells. The scaffolds were then c via two means FESEM analysis as well as fluorescence imaging. In brief, the scaffolds were first treated with Calcein AM dye (Sigma-India, 4 µM in PBS) for 30 min and directly analyzed using a fluorescent microscope (Zeiss) with an excitation filter of 450–490 nm. For FESEM analysis, after washing with PBS, the cells on the scaffolds were first fixed with 4% paraformaldehyde in PBS for 24 h. Then, the scaffolds were washed multiple times with PBS followed by stepwise dehydration with 30%, 40%, 50%, 60%, 70%, 80%, 90%, and 100% concentration gradient of ethanol for 10 min each. Finally, the critical point drying was performed by treating the scaffolds with hexamethyldisilazane (HMDS) for 10 min prior to attachment over the carbon tape for FESEM analysis.

In addition, the scaffolds were analyzed for their cytotoxicity using MTT assay. In brief, the UV sterilized SCA-0, HSCA-2.5, HSCA-5, SCA-2.5, and SCA-5 scaffolds were soaked separately in the serum-free DMEM free media for 24 h at 37 °C. After 24 h, the supernatant was collected and filtered using a 0.22 µm filter. The media was termed as 'conditioned media'. 100 µL of this conditioned media was supplemented to the previously grown MG-63 cells (5000 cells/well in 24 well plates). The conditioned media was changed every alternate day. The MTT assay was then performed at respective days for the cytotoxicity analysis.

All the experiments were performed in triplicates, and the data are reported as average values along with standard deviations.

Results

As discussed in Sect. 2.2, the synthesized ZFHAp samples were dried at 80°C followed by sintering at 650 °C in order to obtain the Ca + Zn + Fe/P ratio of 1.67 (Ca/P = 1.67 for HAp) for mimicking the HAp phase. The HAp phase is addressed as the most suitable phase of calcium phosphate for bone tissue engineering (Saxena et al. 2019). The samples were

further subjected to various chemical characterizations to confirm the synthesis as follows.

Phase structures analysis of ZFHAp

The phase analysis of the sample was analysed using XRD. The obtained XRD pattern was compared with the standard HAp, ZnO, and Fe_3O_4 JCPDS data as shown in Fig. 1a. The XRD patterns reflected the major peaks at 2θ values of 22.61°, 26.34°, 28.41° 33.83°, 34.60°, 49.67° and 53.22° corresponding to the hexagonal HAp (JCPDS 98–007-7606). In addition, XRD peaks at 2θ values of 35.66°, 49.20° and 56.12° corresponded to the hexagonal wurtzite structure of ZnO (JCPDS 98–002-8858). The coinciding peak at 32.15° and 34.60° of HAp and Fe_3O_4 (JCPDS 98–001-7122) and no separate Fe_3O_4 peak exhibited successful doping of Fe into the ZnO (FZO) as reported previously (Saxena and Pandey 2020) followed by its integration with HAp. The crystal size of the sample was calculated using the Scherrer equation (Raland and Borah 2016) and was found to be 68.06 nm.

The XRD patterns also reflected the redshift of major peaks at 2θ values of 26.34°, 28.41° 33.83°, 34.60°, and 49.67°, corresponding to the hexagonal HAp, from 25.86°, 28.2°, 33.7°, 34.52° and 46.74°. This redshift was supposed to be the result of the crystal distortion because of the doping of Zn and Fe into HAp lattice. As the ionic radii of Zn^{2+} (0.074 nm) and Fe^{3+} (0.006 nm) ions is smaller than Ca^{2+} ions (0.231 nm), it can lead to the displacement of Ca^{2+} ions, causing the decrement in the bond length (Saxena et al.2018a; Saxena and Pandey 2020) and a redshift in XRD pattern. Thus, the redshift from standard HAp (Fig. 1b) also reflected the successful integration of FZO with HAp.

The successful synthesis of ZFHAp was further confirmed by evaluating the Raman spectra of the sample. A sharp peak at 960 cm^{-1} corresponding to the Raman shift of phosphate groups (Cuscó et al. 1998) in HAp. The characteristic vibrational peaks of ZnO at 438 cm^{-1} correspondings to E2 (high) (Hansen et al. 2017) blue-shifted to 430 cm^{-1}. A peak corresponding to Fe–O bond at wavenumber 580 cm^{-1} was also obtained. The Raman data complemented the results obtained from the XRD analysis. Hence, the XRD together with Raman data confirmed the successful integration of FZO with HAp, while HAp was the major phase (matrix) of the nanocomposite Fig. 1c. The ZFHAp samples resulted in a colloidally stable solution under neutral pH. HAp has been found to be a colloidally stable solution with a zeta potential value of -22 mV (Lu et al. 2019), similarly Fe(III) doped ZnO has also been found to a colloidal stable in solution with a zeta potential value of + 32.6 ± 1.35 mV (Saxena and Pandey 2020). Hence, their composite was expected to be colloidal stable at neutral pH.

Morphology and elemental analysis

The morphology and the particle size calculations were done using FESEM analysis. The FESEM data revealed that ZFHAp samples comprised of a dual morphology, *i.e.,* the rod shaped as well as spherical morphology. The rod-shaped nanoparticles were found to be 81.78 ± 10 nm in width (Red circled; Fig. 2a), while the spherical nanoparticles were 56.5 ± 14 nm in diameter (Yellow circled; Fig. 2a), probably due to dual phases in the sample, i.e. HAp and FZO as indicated by XRD data. The particles were agglomerated probably due to the experimental sample preparation procedure, *i.e.,* dispersion in water and drying directly on a carbon-coated SEM stub. The elemental analysis was performed using the same FESEM instrument. The primary elements in ZFHAp samples were Ca, P, and O, and the minor elements were Zn and Fe, as shown in Fig. 2b. The ZFHAp conquered Ca:P:O:Zn:Fe as 33.5:16.4:40.3:7.1:2.6 (wt %), which were in linear co-relation with the theoretical values of $Ca_{8.5}Zn_{1.0}Fe_{0.5}(PO_4)_2(OH)_2$ (32.8:17.95:40.18:6.31:2.69) with R^2 = 0.99 as given in Fig. 2B. Similarly, in TEM analysis, a dual morphology was observed, reflecting the diameter of rod-shaped particles as 78.68 ± 8 nm and the diameter of spherical morphology as 49.74 ± 14 nm, respectively (Fig. 2d). The elemental mapping from TEM imaging also corresponded to the theoretical weight percentage of different elements present (Fig. 2B). Further, as shown in Fig. 2e, a dual d-spacing was observed with 0.21 and 0.61 nm of the fringe sizes, indicating the dual morphology of the designed nanomaterial. The atomic ratio of (Ca + Zn + Fe/P) was found to be ∼ 1.7, which corresponded to the Ca/P ratio (1.67) of HAp (Saxena et al. 2018b). The HAp phase depends on the dopant (i.e., ZnO) concentration as well as on the calcination

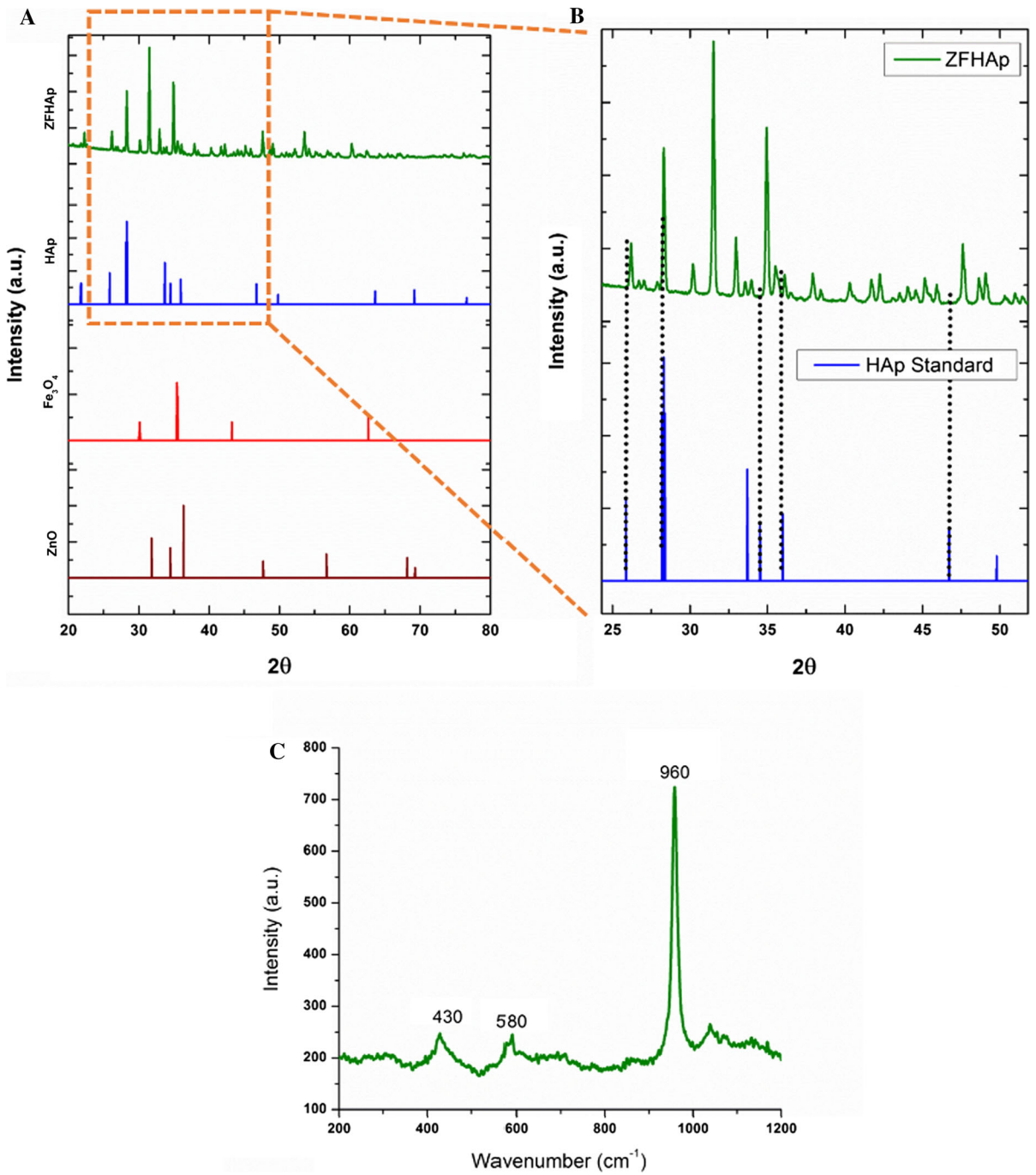

Fig. 1 **a** XRD diffractogram of ZFHAp sample along with the standard HAp (JCPDS 98–007-7606), ZnO (JCPDS 98–002-8858), and Fe_3O_4 (JCPDS 98–001-7122) patterns; **b** Redshift in XRD pattern of ZFHAp samples with Standard HAp (JCPDS 98–007-7606), **c** Raman spectra of ZFHAp reflecting peaks corresponding to phosphate group at 960 cm^{-1}, Zn–O bond at 438 $cm^{-1}$and Fe–O bond at 580 cm^{-1}

temperature (Saxena et al. 2018b); hence suitable co-ordination between them is required for maintaining the HAp phase. The data revealed that after integrating FZO with calcium phosphate, the HAp phase was

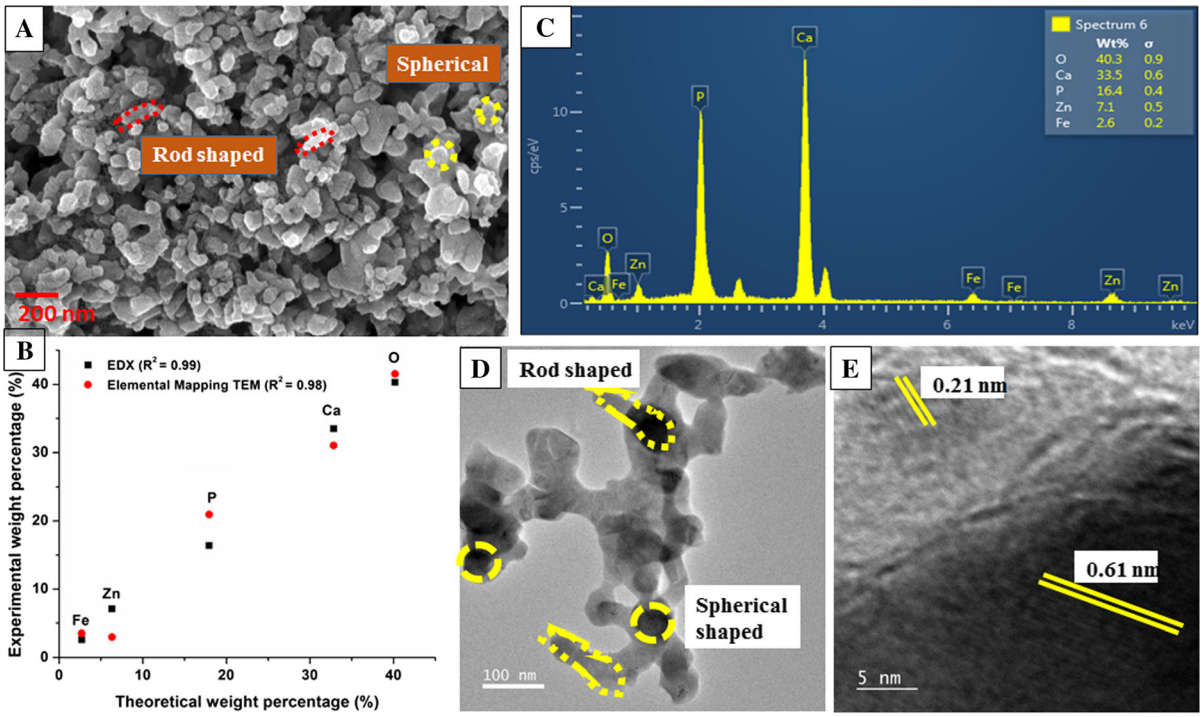

Fig. 2 **a** FESEM image, **b** Co-relation between the experimental and theoretical weight percentage of different ions, **c** EDX analysis of the prepared ZFHAp samples, **d** TEM image of ZFHAp sample indicating the dual morphology, *i.e.,* rod-shaped and particulate shaped, and **e** lattice fringe pattern indicating high crystallinity

maintained in ZFHAp samples. The EDX data complemented the XRD and Raman data indicating HAp as the major phase with FZO integrated within it.

Morphology and pore size analysis of the scaffolds

The scaffolds were analyzed to obtain the morphology with respect to the integration of HAp and ZFHAp samples. FESEM analysis was carried out to examine the internal morphology of the scaffolds. All the samples exhibited microporous architecture, as shown in Fig. 3, while pore sizes were varied for the different samples. The pore size of the microporous structures plays a critical role in regulating the bio-interfacial aspects (cell infiltration, adhesion, cell signalling, angiogenesis, and nutrient exchange) (Hasan et al. 2018b). A well interconnected mesoporous structure was obtained for all the samples, probably due to the crosslinking between amino groups of the chitosan and carboxyl group of CMC and solid–liquid phase separation (Cao et al. 2011). Apparently, the aggregation of particles or the formation of clumps was not observed (Fig. 3), which indicated the good dispersion of HAp and ZFHAp throughout the scaffolds. With the increase in HAp and ZFHAp concentrations, the scaffolds were found to be packed more densely, as shown in Fig. 3. The pore size of the samples was found to increase with the increase in HAp and ZFHAp concentration, as listed in Table 2. The pore size of HAp integrated samples was found to be lesser than that of the ZFHAp integrated scaffolds. Also, the HAp integrated scaffolds carried homogeneously distributed pores as compared to the ZFHAp integrated scaffolds, presumably due to the dual morphology of the ZFHAp samples, which caused the distortion in the mesoporous structure of the scaffolds (Spath et al. 2015). The increase in the pore size is also attributed to the increased concentration of ZFHAp. Covalent bonding between its OH groups of HAp and NH_2 groups of chitosan as well as the co-ordination bonding, are reported in their composites (Venkatesan et al. 2012). Presumably, with an increase in the concentration of ZFHAp, these bonds were increased, which interfered with the chitosan (amine group) and CMC (COOH) group interactions. This resulted in increasing the pore size via solid–liquid phase

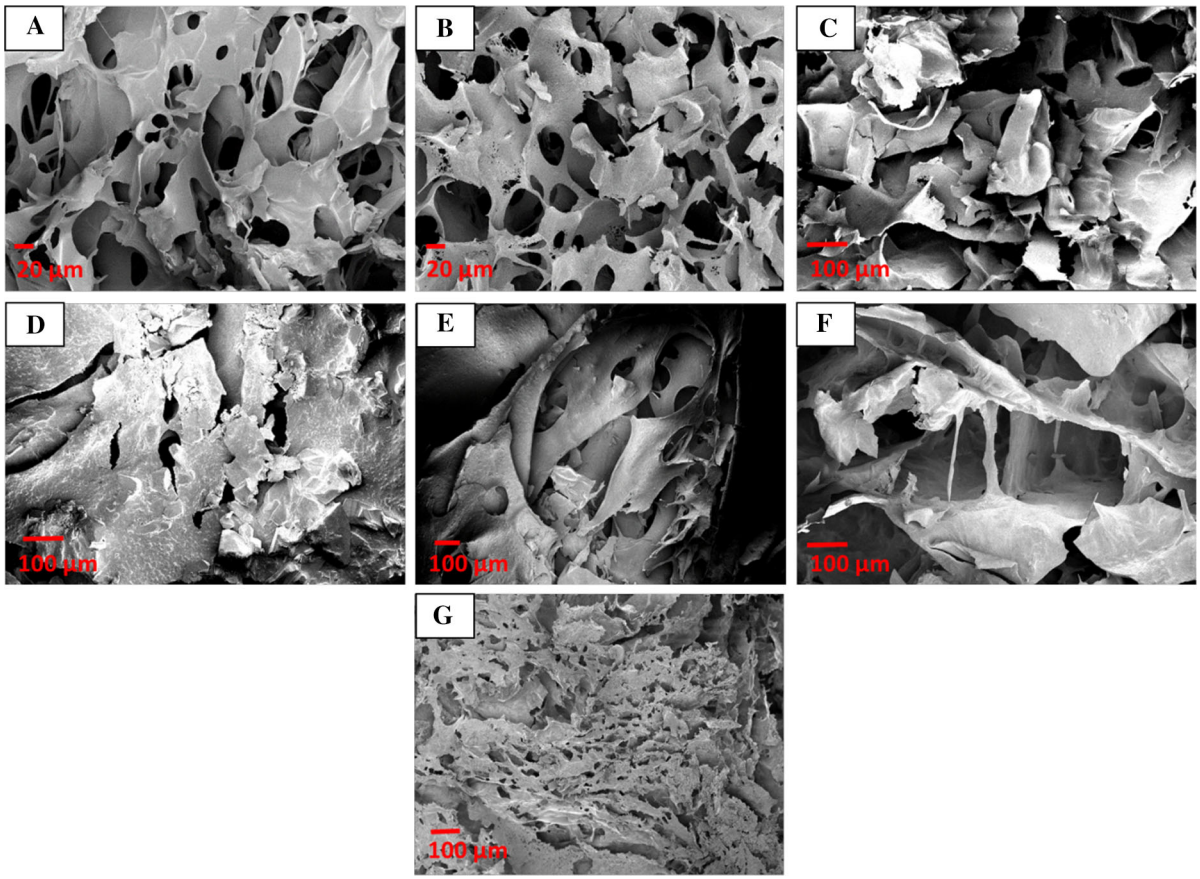

Fig. 3 Morphological analysis of the scaffolds using FESEM; **a** SCA-0, **b** SCA-1, **c** SCA-2, **d** SCA-2.5, **e** SCA-5.0 and **f** SCA-10, **g** HSCA-2.5; Scale bar represents 100 µM

Table 2 Pore size, degradation, and swelling behavior of the ZFHAp integrated scaffolds

S.N	Scaffold sample	Pore size (µm)	Degradation		Swelling		
			k_d(day^{-1})	T_{50} (days)	Q_e	$k_s \times 10^3$(gg^{-1} min^{-1})	R^2
1	SCA-0	25 ± 4	0.045	16	1003	2.24	0.99
2	SCA-1	35 ± 4	0.036	19	949	2.71	0.99
3	SCA-2.5	89 ± 8	0.027	26	738	1.33	0.99
4	SCA-5	92 ± 10	0.017	42	706	0.98	0.99
5	SCA-10	123 ± 28	0.013	53	597	1.53	0.99
6	HSCA-2.5	12 ± 3	0.033	21	802	0.90	0.99

separation (Ghalia and Dahman 2016). Notably, the pore size of cancellous bone lies 300–600 µm in diameter and cortical bone as 10–50 µm (Lee et al. 2012). However, it is reported that the threshold pore size for bone growth remains to be 100 µm (Itälä et al. 2001). In this study, all the scaffolds resulted in the pore size in the same range, affixing their suitability for bone tissue engineering.

Biochemical characterization of scaffolds

The successful synthesis of scaffolds was accessed through its biochemical behavior for biomedical applications. Biological responses to the implant materials depend on various material properties, among which biochemical properties play a significant role. Considering the importance of these properties, the porosity, swelling, and degradation behavior of the scaffolds were analyzed as reported in the following sub-sections.

Porosity

The major challenge in designing a scaffold for bone tissue engineering remains its porosity while maintaining its swelling and degradation behavior. Chitosan, due to its crosslinking with CMC, provides the desired microporous behavior (Mittal et al. 2018). However, controlling the porosity remains a significant challenge for various biomedical applications, especially in bone tissue engineering. A decrease in the porosity was observed by the systematic increase in the concentration of ZFHAp in the scaffolds' composition. Interestingly, the porosity of the HSCA-2.5 was found to be lower than that of SCA-2.5, as compared to its morphology, presumably due to the different packings of the HAp and ZFHAp within the scaffolds (Fig. 4a). For instance, SCA-0 exhibited 95% porosity, which was significantly reduced to ∼ 60% for all the HSCA samples. However, the porosity was found to be 88% in SCA-1 (1% addition of ZFHAp). Likewise, the porosity further decreased to the range of 68%—75% upon the increase in ZFHAp concentrations. The least porosity of 58% was observed for the scaffold with the maximum amount of ZFHAp (SCA-10) (Fig. 4a). A similar pattern, *i.e.*, the decrease in porous morphology, can be seen in Fig. 3. Hence, the measured porosity supported the results obtained through the morphological analysis of the scaffolds. The decreased porosity can be ascribed to the high concentration of ZFHAp with dual morphology, *i.e.,* rod-shaped and particulate. The HAp NPs carried single particulate morphology and hence were mixed homogenously with the Chitosan and CMC and did not cause any change at an increase in their concentration. The packing of dual morphology of ZFHAp increases the heterogeneity and hence presumably regulates the density, interconnectivity, and orientation of the designed scaffolds. The osseointegration has been reported to be best observed at 60–80% of porosity, which is similar to the porosity of the cancellous bone (Hasan et al. 2018b). Based on the results, porosities were obtained in this desired range for all HSCA-2.5 scaffolds and SCA-2, SCA-2.5, and SCA-5 scaffolds. It is to be noted that the porosity can be controlled by varying the concentrations of ZFHAp. This provides an advantage of tuneable porosity, which is also expected to alter the scaffolds' swelling behavior.

Swelling behavior

Similar to the porosity, controlling the swelling behavior is also crucial for maintaining the integrity and fidelity of the scaffolds upon interactions with the biological fluids. However, the swelling of scaffolds is originated from the native properties of the constituent materials, *i.e.,* Chitosan, CMC, HAp, and/or ZFHAp. This enables to control the swelling ability at the

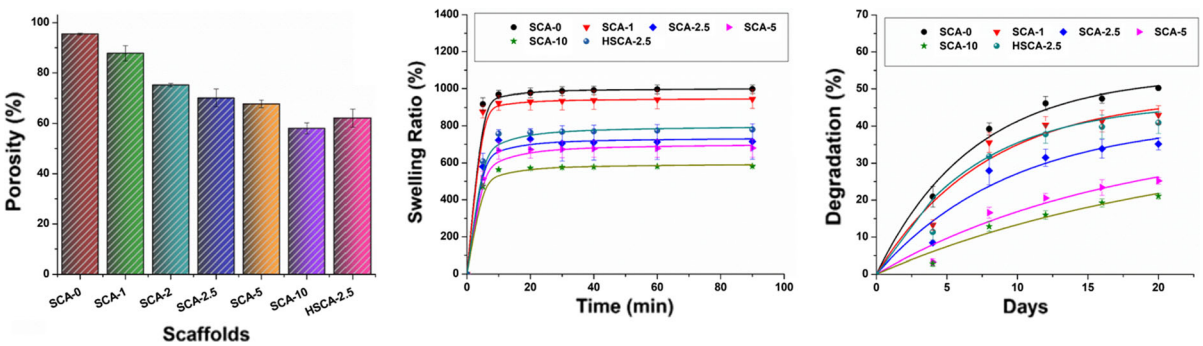

Fig. 4 Biochemical characterizations of the ZFHAp integrated scaffolds; **a** porosity, **b** % Swelling, **c** Degradation studies. Points are the experimental data, while lines refer to the fitted data

material selection level. In this study, the swelling behavior was evaluated via immersing the scaffolds into the PBS at 37 °C. It was found that the swelling behavior decreased with an increase in ZFHAp concentration, as shown in Fig. 4b. The obtained experimental data were fitted to the second-order swelling kinetics model (Eq. 8). The experimental data fitted well the second-order kinetics (R^2 = 0.99), while the data did not fit with the first-order kinetics. This indicated that the swelling behavior is affected by the diffusion of the water along with the intermolecular interactions between the constituents of the scaffolds. The fitted kinetic parameters are listed in Table 2, which indicated that the scaffolds' swelling capacity decreased with an increase in the concentration of ZFHAp due to the reduction of H-bonds between chitosan and CMC (Berger et al. 2004). The swelling behavior of HSCA-2.5 was found to be in between the SCA-1 and SCA-2.5. This indicated that the morphology and the concentration of the HAp and ZFHAp nanomaterials could be effectively used for controlling the biochemical nature of the scaffolds. The rate constant k_s was also found to decrease with the increase in the contents of HAp/ZFHAp; however, the k_s Values were higher for the ZFHAp based scaffolds. ZFHAp interacted with the Chitosan and CMC with different physical (Van der Waals) and chemical bonds, which resulted in the decreased fluid intake capacity of the scaffolds. The reduced swelling behavior is desirable for the controlled degradation of scaffolds for various biomedical applications, including drug delivery and bone tissue engineering applications. Hence, SCA samples containing ZFHAp NPs are better suited for these applications than the HSCA samples.

Enzymatic degradation

Enzymatic degradation is one of the key factors for the performance of scaffolds in biological fluids. Various enzymes such as lysozymes are found abundant in body fluids. The lysozymes' antibacterial activity is reported as the first line of defense against bacterial infection through the rupturing of the β-1–4-glycosidic linkages of peptidoglycan (Benbow et al. 2020). Chitosan also undergoes catalytic degradation over its β-1–4-glycosidic linkages by the action of lysozyme. Hence, the stability under such body fluids is a significant challenge in designing the implant materials. The degradation of β-1–4- glycosidic linkages in chitosan by lysozyme's action, is found to loosen the interactions between Chitosan and CMC, which resulted in collapsing of the scaffold microstructure (Hasan et al. 2018b). The deprotonation under PBS incubation may also weaken the electrostatic interactions between Chitosan/CMC and HAp/ZFHAp. However, it has been observed that the scaffolds made up of various polymers containing HAp exhibited negligible degradation. For example, HAp/polycaprolactone scaffolds degraded only 3.7% in 10 weeks (Wang et al. 2010), and no significant degradation was reported in carbon fibre reinforced HAp/polylactide biocomposite scaffolds even in 12 weeks (Shen et al. 2009). Therefore, we performed enzymatic degradation in PBS containing lysozymes. In this study, a higher degradation rate for SCA-0 was obtained as compared to other scaffolds containing HAp and ZFHAp (Fig. 4c, Table 2). The degradation was found to be in the range of 21–50%, depending on the physical and chemical characteristics of the scaffolds. SCA-0 scaffolds resulted in a degradation of 50%, which was consistent with the previous studies (Hasan et al. 2018b). However, the increase in the HAp and ZFHAp concentration resulted in the augmented form of the co-ordination bonds between chitosan-HAp, and chitosan-ZFHAp particles, respectively, which prevented and retarded the degradation activity of lysozymes. Thus we observed a faster degradation of scaffolds without (SCA-0) or with less content of HAp and ZFHAp (SCA-1, SCA-2) as compared to SCA-5 and SCA-10. However, the degradation rates of HSCA samples were higher than that of SCA samples at the same concentration. For examples, the degradation behavior of HSCA-2.5 was comparable with SCA-1 (Table 2). This observation indicated the presence of fewer co-ordination bonds of nano-HAp with Chitosan and CMC as compared to ZFHAp.

Table 2 listed the fitted data obtained using Eq. 10. The degradation rate k_d was found to decrease with an increase in the concentration of HAp/ZFHAp. T_{50} values were also estimated as $\ln 2/k_d$, which was found to be significantly enhanced with the increase in HAp/ZFHAp concentrations. It has been reported that the bone formation starts at the corner of the scaffolds in the initial 0–10 days, followed by no bone formation for 10–20 days (only changes in scaffolds). Later bone

formation occurs along with scaffold degradation up to 90 days and becomes thicker with whole scaffold degradation within 90 to 150 days (Adachi et al. 2006). The study suggested the role of dense and oriented bone formation at a slower scaffold degradation rate. In this study, the T_{50} degradation for SCA-5 was found to be 42 days (6 weeks), signifying its excellent bone formation ability.

The dual morphology of ZFHAp samples affects the packing and density of Chitosan and CMC. Additionally, the uniformly distributed ZFHAp alters the crosslinking sites and the nature of the bond formations between Chitosan and CMC. Various ionic and van der Waals interactions take place between the three constituents of scaffolds, *i.e.*, Chitosan, HAp/ZFHAp, and CMC. For example, the NH_2 groups of Chitosan and OH groups of HAp form bonds, altering the porosity as well as the degradation rate of the scaffolds. Similarly, the HAp has been reported to form covalent bonds with the CMC (Grande et al. 2009), altering the swelling and degradation behavior of the scaffolds. In this study, incorporation of ZFHAp is presumed to delay the degradation rate due to synergistic effects of the chemical interactions between the NH_2 groups of chitosan and the carboxyl group of CMC, co-ordination bonds between Ca, Zn, and Fe with Chitosan, and ionic interactions with the carboxyl groups of CMC.

Mechanical strength analysis of the scaffolds

The mechanical strength of scaffolds is an essential parameter for the integrity as well proliferation of the bone cells. Hence, the mechanical strength of the selected scaffolds (HSCA-2.5, HSCA-10, SCA-2.5, and SCA-10) was examined as given in the material and methods section. The mechanical strength parameters are given in Table 3. HSCA samples exhibited a higher elastic modulus as compared to SCA samples because of their lesser porosity. The maximum tolerance against the applied force was observed for the HSCA-10 sample as the scaffold was not deformed until 0.72 MPa of the force applied per the 3.14 cm^2 area. This indicated that the dual morphology of the ZFHAp samples caused the maximum distortion and heterogeneity, which compromised the mechanical strength of the SCA scaffolds (Spath et al. 2015). It has been reported that the compressive strength of the trabecular bone remains in the range of 0.1–16 MPa (Gerhardt and Boccaccini 2010); in this study, the compressive strength was found to be in the above range affirming the suitability of the scaffolds without any stress shielding effect. It is to be noted that the scaffolds with a faster degradation rate exhibited a lower mechanical property.

Table 3 Mechanical strength analysis of the scaffolds

Sample	E_{mod} (MPa)	F_{max} (MPa)
HSCA-2.5	0.27	0.25
HSCA-10	0.72	0.33
SCA-2.5	0.17	0.24
SCA-10	0.32	0.16

Antibacterial activity analysis

HAp is considered the most suitable inorganic material for bone tissue engineering because of its physical and chemical properties similar to bone. However, the lack of inherent antibacterial activity remains a significant challenge for biomaterial researchers (Saxena et al. 2018b). For this purpose, we integrated FZO with HAp. The major challenge for this study was to obtain the desired antibacterial activity after the integration of ZFHAp with Chitosan. For this purpose, the antibacterial activity of nanocomposite scaffolds, SCA-0, SCA-2.5, and SCA-5, HSCA-2.5, and HSCA-5 was tested against Gram-negative (*E. coli and S. paratyphi*) and Gram-positive (*S. aureus and L. monocytogenes*) bacteria. As presumed, SCA-0 did not show any antibacterial activity, and densely packed bacterial colonies (fully covered plates) were observed (Fig. 5).

Similarly, for SCA-2.5, a reduction in the bacterial colony as a visible decrease is seen in Fig. 5. Although a considerable number was decreased, yet the bacterial colonies were spread all over the agar plate. For SCA-5, no bacterial growth was observed (Fig. 5), affirming its suitability for antibacterial action. It is to be noted that HAp does not carry antibacterial activity by itself, and thus no antibacterial activity could be obtained for HSCA-2.5 and HSCA-5. Hence the antibacterial activity of the scaffolds can be attributed to the integration of Zn^{2+} and Fe^{3+} ions to the HAp lattice. Chitosan is reported to exhibit antibacterial activity at

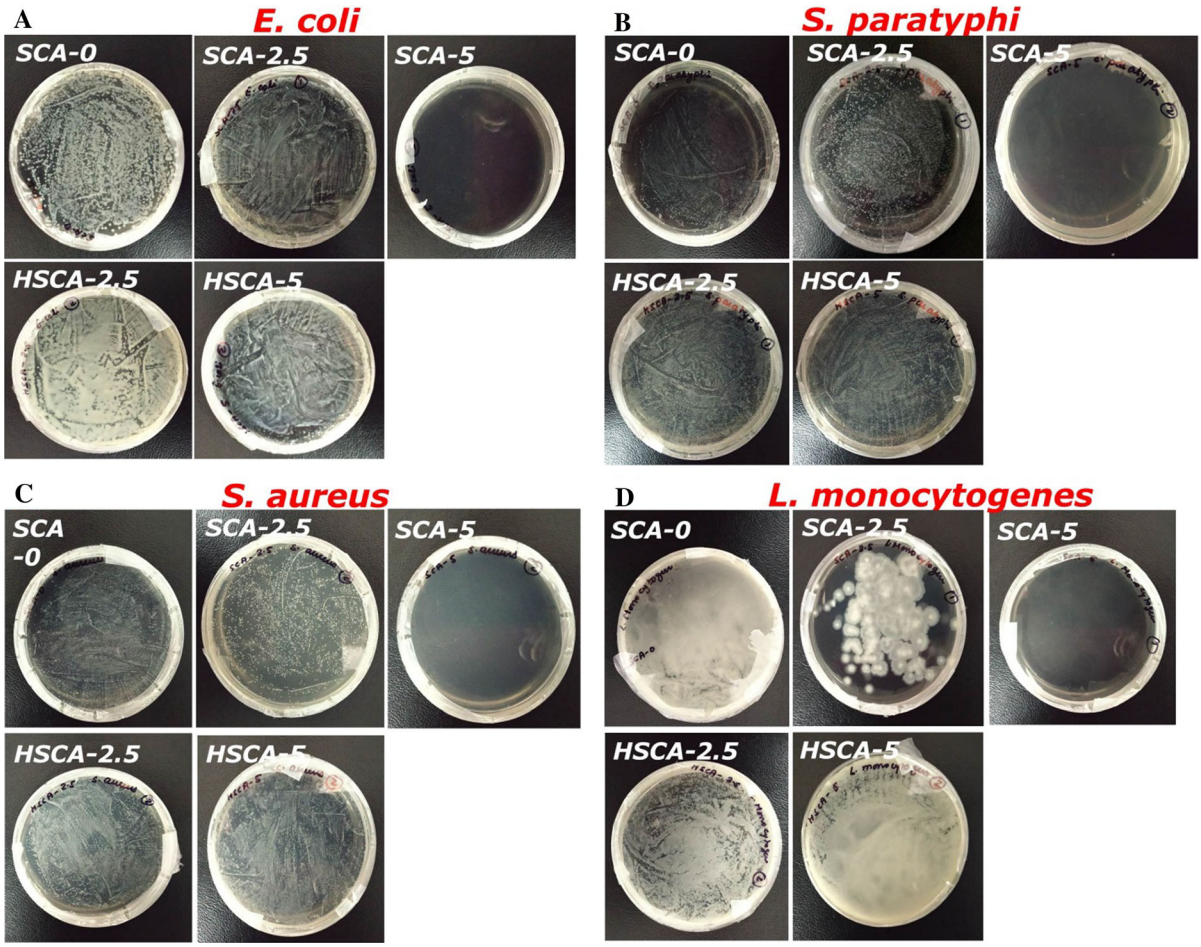

Fig. 5 Antibacterial activity of scaffolds SCA-0, SCA-2 and SCA-5, HSCA-2.5 and HSCA-5 against *E. coli* **a,** *S. paratyphi* **b,** *S.aureus,* **c,** and *L. monocytogenes* **d,** respectively

a higher concentration (Fei Liu et al. 2001). In a previous study, we have reported the antibacterial activity of FZO against pathogenic bacteria through the release of Zn^{2+} and Fe^{3+} ions. The MIC values for the FZO NPs were found to be $\sim$ 33 µg/mL (Saxena and Pandey 2020). Additionally, the contact inhibition of the bacterial growth was supposed to take place. The SCA-5 completely inhibited bacterial growth. This observed antibacterial activity can be attributed to the slower and controlled degradation of the SCA-5, providing the desired bactericidal concentrations of the Zn^{2+} and Fe^{3+} ions.

Cell proliferation analysis of MG-63 (bone like) cells

The designed scaffolds were analyzed for their bone cell proliferation ability using FESEM and fluorescence microscopy. Human bone-like cells, MG-63, were seeded over the SCA-5 to analyze the bone cell formation ability of the scaffolds. As we identified the best response of the SCA-5 against bacterial cells, the same scaffold sample was further tested for *in-vitro* cell proliferation applications. The FESEM images for the MG-63 cells adhered to the scaffolds for five days were recorded as shown in Fig. 6a. The results demonstrated that the MG-63 cells adhered well and penetrated inside the microporous structure of SCA-5. To analyze the cell proliferation, cells grown for five days on SCA-5 were treated with Calcein-AM dye and

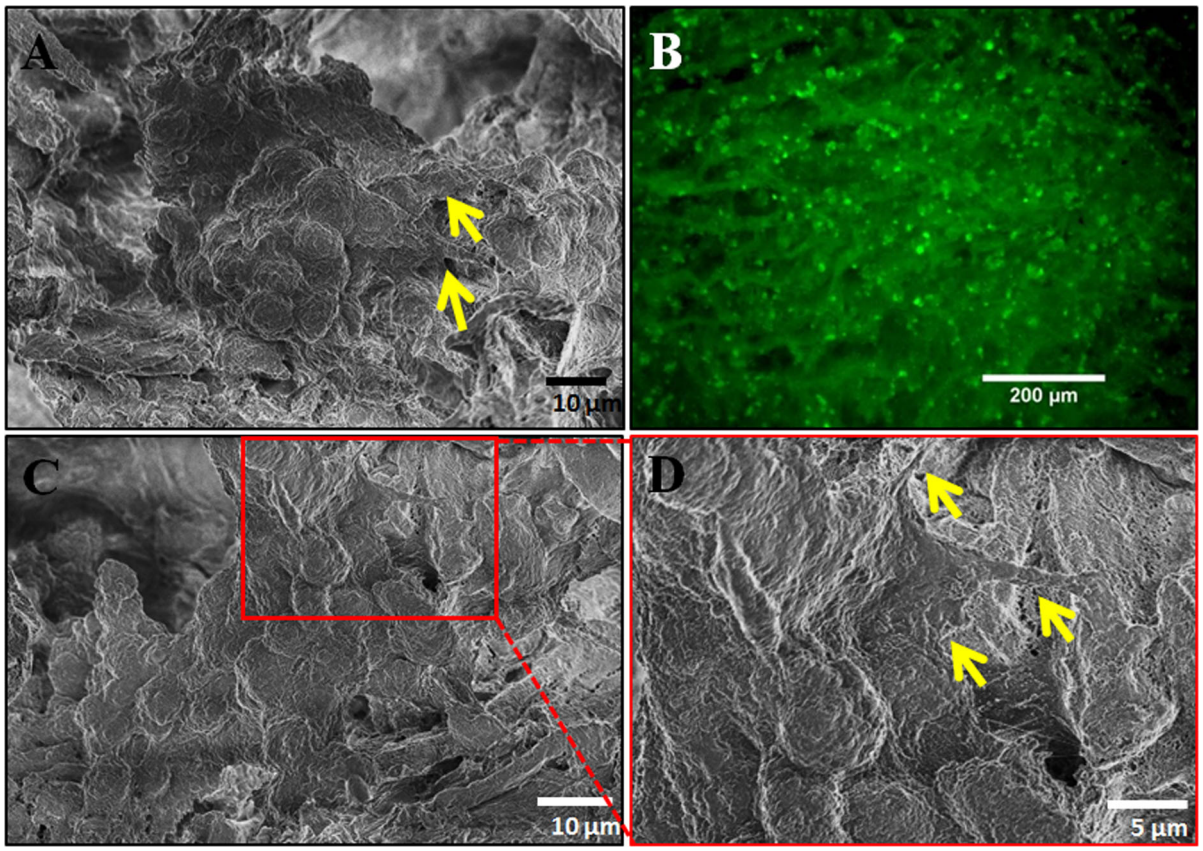

Fig. 6 The attachment and proliferation of MG-63 cells on scaffolds. **a** FESEM image of cells on SCA-0, **b** Fluorescence image of cells adhered on SCA-5, **c**, and **d** FESEM image of cells on SCA-5 scaffold. Arrows in image a and d show cells filipodia indicating cell attachment

monitored using an inverted fluorescent microscope. The bright green spots under the fluorescence microscopy image (Fig. 6b) represent the population of adhered and proliferating cells. Higher magnification images of all the scaffolds with adhered cells (Supplementary Fig. S1) and the estimation of cell area (μm^2) and cell circularity (Supplementary Fig. S2) indicated the cell spreading. The circularity of adhered cells defines the shapes of the cell (Hasan et al. 2018a). Non-adhered cells exhibit round morphology with circularity = 1, whereas the lower value of circularity (*i.e.,* circularity < 1) signifies better cell spreading with more focal points which leads to a change in the cell shape. The circularity values calculated for adhered cells on all the scaffolds (Supplementary Fig. S2) were observed to be less than 0.85 thus indicating cell spreading.

The interfacial interaction between the scaffold and the cells can be attributed to its bone-like chemical configuration due to the presence of Chitosan and HAp as major constituents and Zn and Fe as trace mineral components. It has been previously reported that the presence of Zn and Fe also promotes better interaction between cells and underlying bone tissue (Saxena et al. 2019). Additionally, our group previously reported that the MG-63 cells exhibited ~ 100% viability after days 2, 4, and 6 days; when cultured on the composite scaffolds prepared using chitosan, carboxymethyl cellulose, and silver nanoparticle modified cellulose nanowhiskers (Hasan et al. 2018b). Hence, ZFHAp nanocomposite uniformly distributed within chitosan might have provided a suitable microenvironment for bone cells' growth.

In addition to the cell proliferation analysis, the cytotoxicity analysis of HSCA and SCA samples was carried out, as described in the materials and method section. To analyze the toxic effect of degradation by-product of the scaffolds, the conditioned media was

supplemented to the MG-63 cells. The MTT assay analysis after 1, 3, and 6 days revealed no significant decrease in both HSCA and SCA scaffolds. The cells were found to be ∼ 99% viable as compared to the control cells (Cells grown in DMEM media; Fig. 7). This confirmed that HSCA and SCA scaffolds did not exhibit any cytotoxicity up to 6 days of incubation.

In summary, various physical, chemical, and biological properties of the prepared scaffolds have been tuned by varying the contents of ZFHAp. The porosity of the scaffold controls the swelling behavior as well as the enzymatic degradation of the scaffolds. As shown in Fig. 8, the scaffolds' porosity was found to be directly correlated with the degradation and the swelling behaviors. Linear correlations between the porosity and enzymatic degradation with an R^2 value of 0.92 and porosity and % swelling with an R^2 value of 0.99 were observed, indicating that the porosity governed the swelling and enzymatic degradation. Hence, it was confirmed that the ZFHAp concentrations directly affected the porosity of the scaffolds, leading to control over its other biochemical behaviors. Hence, along with the controlled swelling and porous behavior, a slower degradation rate was observed (Fig. 4). The presence of ZFHAp also imparted antibacterial properties to the scaffolds (Fig. 5). The controlled degradation provided an excellent antibacterial activity to the scaffold (∼ 100% cell death) and provided better cell attachment and growth.

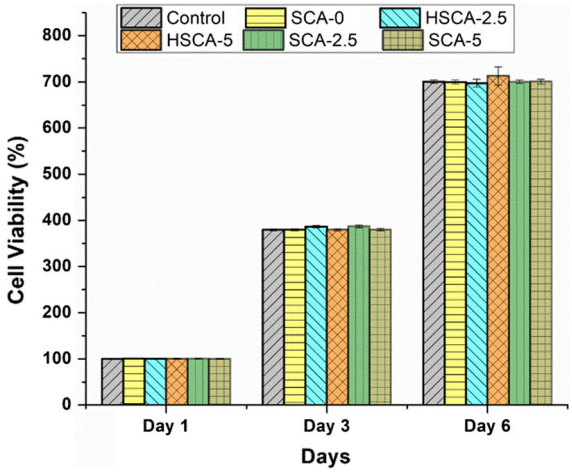

Fig. 7 Cell proliferation analysis of the HSCA and SCA scaffolds for 1, 3, and 6 days

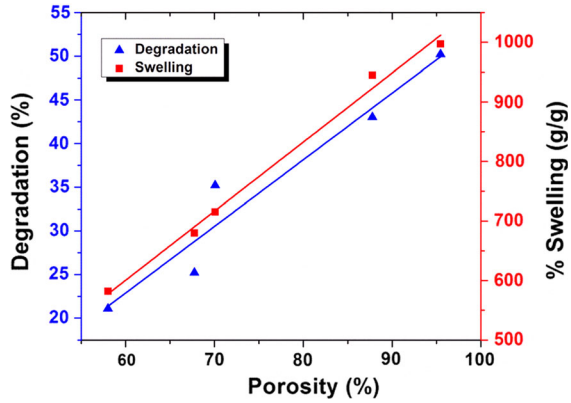

Fig. 8 Linearly fitted data of correlation between co-relation between porosity, degradation and swelling behavior

Various studies have been performed on chitosan-based scaffolds for the controlled bone tissue engineering and are listed in Table 4. A study reported the excellent swelling behavior and the required microporous structure of the scaffolds but with a higher degradation rate, *i.e.,* 50% degradation in 28 days (Kozlowska et al. 2019). Few studies utilized HAp as a constituent for the scaffold, yet their degradation was higher (Table 4). This can be explained by the bond formation between HAp and Chitosan. However, the antibacterial activities in the Chitosan-HAp based scaffolds were not observed. In this study, the ZFHAp contained three electron donor groups, *i.e.,* Ca, Fe, and Zn that form the co-ordination bonds between HAp and Chitosan. With the increase in ZFHAp concentrations, the number of coordinate bonds was increased, and the scaffolds remained unaffected by the enzymatic degradation.

On the other hand, the integration of Zn and Fe to HAp prior to the scaffold formation provided an excellent antibacterial activity to the scaffolds. The concentration-dependent controlled degradation, excellent antibacterial activity, along with the desired swelling behavior, porosity, and mechanical strength, enable these scaffolds to be the potential candidates for bone tissue engineering applications. Hence, this study designates the SCA-5 as plausible scaffolds for orthopedic applications.

Table 4 Recent advances in chitosan based scaffolds

S. n	Scaffolds	Swelling ratio (%)	Porosity (%)	Degradation (%)	Antibacterial activity	Ref
1	nanoHAp/Chitosan/CMC	NA	77.8	30% (after 30 days)	NA	(Liuyun et al.2009)
2	nanoHAp/Chitosan/CMC	NA	~ 72–80	10–12% (after 56 days)	NA	(Jiang et al. 2008)
3	Chitosan/HAp	1300–2200	84–91	NA	NA	(Rogina et al. 2016)
4	Agarose/Chitosan/Graphene oxide	2640–2930	73–79	43–45% (after 28 days)	NA	(Sivashankari and Prabaharan 2020)
5	Clinoptilolite-nanoHAp/Chitosan/Gelatin	1200–1800	79–98	28–56% (after 21 days)	NA	(Sadeghinia et al.2020)
6	Chitosan/Silk protein	200–300	77–85	29–50% (after 28 days)	NA	(Wang et al.2020)
7	Chitosan/CMC/reinforced with multiphasic Calcium Phosphate	600–1500	61–75	NA	NA	(Matinfar et al.2019)
8	Collagen/Chitosan Poly (ethylene glycol)/nanoHAp	1150–1400	75–84	40–73%	NA	(Kozlowska et al. 2019)
9	Chitosan/CMC/mesoporous wollastonite	1800–2200	NA	~ 50–80% (after 14 days)	NA	(Sainitya et al.2015)
10	Chitosan/Carboxymethyl cellulose/Silver nanoparticles modified Cellulose nanoWhiskers (CCNWs-AgNP)	584–1070	77–96	21–55% (after 20 days)	100% antibacterial efficiency at 2.5% and 5% of CCNWs-AgNP concentration	(Hasan et al.2018b)
11	Chitosan/HAp	NA	NA	0.5–3% (after 72 h)	NA	(Pu et al. 2013)
12	Chitosan/TCP/HAp	200–800	54–91	13% (after 28 days)	NA	(Shavandi et al.2015)
13	Hydroxypropyl chitosan /nano-HAp/Fucoidan	250–2500	61.5–81.2	10–28% (after 28 days)	NA	(Lu et al. 2019)
14	Chitosan	NA	98–99	2.5–14% (after 14 days)	NA	(Kruppke et al.2017)
15	Chitosan/CMC/ZFHAp	473–997	58–96	21–50% (after 20 days)	~ 100% Antibacterial at 5% concentration of ZFHAp	This Study

NA, Not available; β-TCP, tricalcium phosphate; HAp, hydroxyapatite; CMC, carboxy methyl cellulose

Conclusion

In the present work, we successfully prepared the naturally occurring polymer-nano composite based hybrid scaffolds with concentration-dependent biochemical behaviors. The Fe(III) doped ZnO integrated HAp nanocomposite (ZFHAp) showed excellent control over scaffold's physical and biochemical properties. The dual morphology of ZFHAp and intermolecular interactions altered the packing behaviour and thus controlled the porosity, swelling behaviour as well as the controlled degradation of the scaffolds. The presence of Zn and Fe ions in the HAp lattice also played a crucial role in controlling the porosity, degradation and swelling behaviour of the scaffolds. The presence of these metal ions in HAp lattice not only altered its morphology but also interfered with its charge unbalancing, which affected the interaction with chitosan and CMC to a great extent. The co-ordination bonding of ZFHAp with chitosan and CMC resulted in reduced enzymatic degradation, whereas less co-ordination bond with HAp resulted in rapid degradation as compared to HSCA scaffolds. However, the mechanical strength of the HSCA scaffolds was found to be higher than that of the SCA samples, presumable due to the higher porosity of the ZFHAp samples. The swelling behavior and enzymatic degradation were found to be linearly related to the porosity of the scaffolds. The addition of Zn and Fe to the HAp matrix imparted excellent antimicrobial activity to the scaffolds. In addition, synergistically ZFHAp and chitosan supported the bone cell proliferation ability of the scaffolds. This present study provides an insight into designing the polymeric scaffolds with self-antibacterial properties along with controlled biochemical behaviors.

Acknowledgments Authors are thankful to the Department of Science and Technology, Government of India for their financial supports (Sanction Nos: DST/INSPIRE/04/2014/002020, ECR/2016/001027). Authors are also obliged to the Department of Biosciences and Bioengineering and Central Instruments Facility (CIF) of the Indian Institute of Technology Guwahati (IITG), India for providing all necessary instrumentation facilities.

Declarations

Conflict of interest The author declared that there is no conflict of interest.

References

Adachi T, Osako Y, Tanaka M, Hojo M, Hollister SJ (2006) Framework for optimal design of porous scaffold microstructure by computational simulation of bone regeneration. Biomaterials 27:3964–3972. https://doi.org/10.1016/j.biomaterials.2006.02.039

Atila D, Karataş A, Evcin A, Keskin D, Tezcaner A (2019) Bacterial cellulose-reinforced boron-doped hydroxyapatite/gelatin scaffolds for bone tissue engineering. Cellulose 26:9765–9785. https://doi.org/10.1007/s10570-019-02741-1

Awwad AM, Salem NM, Aqarbeh MM, Abdulaziz FM (2020) Green synthesis, characterization of silver sulfide nanoparticles and antibacterial activity evaluation. Chem Int 6(1):42–48. https://doi.org/10.5281/zenodo.3243157

Baskaran P, Udduttula A, Uthirapathy V (2017) Development and characterisation of novel Ce-doped hydroxyapatite–Fe_3O_4 nanocomposites and their in vitro biological evaluations for biomedical applications. IET Nanobiotechnol 12(2):138–146. https://doi.org/10.1049/iet-nbt.2017.0029

Benbow NL, Sebben DA, Karpiniec S, Stringer D, Krasowska M, Beattie DA (2020) Lysozyme uptake into pharmaceutical grade fucoidan/chitosan polyelectrolyte multilayers under physiological conditions. J Colloid Interface Sci 565:555–566. https://doi.org/10.1016/j.jcis.2020.01.030

Berger J, Reist M, Mayer JM, Felt O, Peppas NA, Gurny R (2004) Structure and interactions in covalently and ionically crosslinked chitosan hydrogels for biomedical applications. Eur J Pharm Biopharm 57:19–34. https://doi.org/10.1016/S0939-6411(03)00161-9

Cao B, Yin J, Yan S, Cui L, Chen X, Xie Y (2011) Porous Scaffolds Based on Cross-Linking of Poly (L-glutamic acid). Macromol Biosci 11(3):427–434. https://doi.org/10.1002/mabi.201000389

Cuscó R, Guitián F, Aza Sde, Artús L (1998) Differentiation between hydroxyapatite and β-tricalcium phosphate by means of μ-Raman spectroscopy. J European Ceramic Soc 18(9):1301–1305. https://doi.org/10.1016/S0955-2219(98)00057-0

Fei Liu X, Lin Guan Y, Zhi Yang D, Li Z, De Yao K (2001) Antibacterial action of chitosan and carboxymethylated chitosan. J Appl Polym Sci 79:1324–1335. https://doi.org/10.1002/1097-4628(20010214)79:7%3c1324::AID-APP210%3e3.0.CO;2-L

Fontenot KR, Nam S, French AD, Condon BD (2019) Stability and Antibacterial Assessment of Copper Nanoparticles Dispersed on Cotton Fabrics. AATCC J Res 6(3):8–19. https://doi.org/10.14504/ajr.6.3.2

French AD, Johnson GP (2009) Cellulose and the twofold screw axis: modeling and experimental arguments. Cellulose 16:959–973. https://doi.org/10.1007/s10570-009-9347-4

Gamiz Gonzalez MA, Edlund U, Vidaurre A, Gomez Ribelles JL (2017) Synthesis of highly swellable hydrogels of water-soluble carboxymethyl chitosan and poly (ethylene glycol). Polym Int 66(11):1624–1632. https://doi.org/10.1002/pi.5424

Gerhardt LC, Boccaccini AR (2010) Bioactive glass and glass-ceramic scaffolds for bone tissue engineering. Materials 3(7):3867–3910. https://doi.org/10.3390/ma3073867

Ghalia MA, Dahman Y (2016) Chapter 6—Advanced nanobiomaterials in tissue engineering: Synthesis, properties, and applications. In: Grumezescu AM (ed) Nanobiomaterials in Soft Tissue Engineering. William Andrew Publishing, pp 141–172. doi:https://doi.org/10.1016/B978-0-323-42865-1.00006-4

Grande CJ, Torres FG, Gomez CM, Carmen Bañó M (2009) Nanocomposites of bacterial cellulose/hydroxyapatite for biomedical applications. Acta Biomater 5:1605–1615. https://doi.org/10.1016/j.actbio.2009.01.022

Guerzoni S, Deplaine H, El Haskouri J, Amorós P, Pradas MM, Edlund U, Ferrer GG (2014) Combination of silica nanoparticles with hydroxyapatite reinforces poly (L-lactide acid) scaffolds without loss of bioactivity. J Bioactive Compat Polym 29(1):15–31. https://doi.org/10.1177/0883911513513093

Hansen M, Truong J, Xie T, Hahm J-i (2017) Spatially distinct Raman scattering characteristics of individual ZnO nanorods under controlled polarization: intense end scattering from forbidden modes. Nanoscale 9(24):8470–8480. https://doi.org/10.1039/C7NR02672B

Hasan A, Lee K, Tewari K, Pandey LM, Messersmith PB, Faulds K, Lau KHA (2020a) Surface design for immobilization of an antimicrobial peptide mimic for efficient anti-biofouling. Chem (weinheim an Der Bergstrasse, Germany) 26(26):5789-5793. https://doi.org/10.1002/chem.202000746

Hasan A, Saxena V, Castelletto V, Zimbitas G, Seitsonen J, Ruokolainen J, Pandey LM, Sefcik J, Hamley IW, Lau KHA (2020b) Chain-end modifications and sequence arrangements of antimicrobial peptoids for mediating activity and nano-assembly. Front Chem 8:416. https://doi.org/10.3389/fchem.2020.00416

Hasan A, Saxena V, Pandey LM (2018a) Surface functionalization of Ti6Al4V via self-assembled monolayers for improved protein adsorption and fibroblast adhesion. Langmuir 34(11):3494–3506. https://doi.org/10.1021/acs.langmuir.7b03152

Hasan A, Waibhaw G, Saxena V, Pandey LM (2018b) Nanobiocomposite scaffolds of chitosan, carboxymethyl cellulose and silver nanoparticle modified cellulose nanowhiskers for bone tissue engineering applications. Int J Biol Macromol 111:923–934. https://doi.org/10.1016/j.ijbiomac.2018.01.089

Itälä AI, Ylänen HO, Ekholm C, Karlsson KH, Aro HT (2001) Pore diameter of more than 100 μm is not requisite for bone ingrowth in rabbits. J Biomed Mater Res 58(6):679–683. https://doi.org/10.1002/jbm.1069

Jiang L, Li Y, Wang X, Zhang L, Wen J, Gong M (2008) Preparation and properties of nano-hydroxyapatite/chitosan/carboxymethyl cellulose composite scaffold. Carbohydrate Polymers 74(3):680–684. https://doi.org/10.1016/j.carbpol.2008.04.035

Kharaghani D et al (2020) Active loading graphite/hydroxyapatite into the stable hydroxyethyl cellulose scaffold nanofibers for artificial cornea application. Cellulose 27:3319–3334. https://doi.org/10.1007/s10570-020-02999-w

Kozlowska J, Stachowiak N, Sionkowska A (2019) Preparation and characterization of collagen/chitosan poly (ethylene glycol)/nanohydroxyapatite composite scaffolds. Polym Adv Technol 30(3):799–803. https://doi.org/10.1002/pat.4506

Kruppke B, Farack J, Sommer F, Weil S, Aflalo ED, Wiesmann H-P, Sagi A, Hanke T (2017) In situ crosslinking of highly porous chitosan scaffolds for bone regeneration: production parameters and in vitro characterization. Macromol Mat Eng 302(10):1700147. https://doi.org/10.1002/mame.201700147

Lee S, Porter M, Wasko S, Lau G, Chen PY, Novitskaya EE, Tomsia AP, Almutairi A, Meyers MA, and McKittrick J (2012) Potential bone replacement materials prepared by two methods. MRS Proceedings 1418. https://doi.org/10.1557/opl.2012.671

Ling Z, Xu F, Edwards JV, Prevost NT, Nam S, Condon BD, French AD (2019) Nanocellulose as a colorimetric biosensor for effective and facile detection of human neutrophil elastase. Carbohyd Polym 216:360–368. https://doi.org/10.1016/j.carbpol.2019.04.027

Liuyun J, Yubao L, Chengdong X (2009) Preparation and biological properties of a novel composite scaffold of nano-hydroxyapatite/chitosan/carboxymethyl cellulose for bone tissue engineering. J Biomed Sci 16(1):65. https://doi.org/10.1186/1423-0127-16-65

Lu H-T, Lu T-W, Chen C-H, Mi F-W (2019) Development of genipin-crosslinked and fucoidan-adsorbed nano-hydroxyapatite/hydroxypropyl chitosan composite scaffolds for bone tissue engineering. Int J Biol Macromol 128:973–984. https://doi.org/10.1016/j.ijbiomac.2019.02.010

Maitra A (2005) Calcium phosphate nanoparticles: second-generation nonviral vectors in gene therapy. Expert Rev Mol Diagn 5:893–905. https://doi.org/10.1586/14737159.5.6.893

Matinfar M, Mesgar AS, Mohammadi Z (2019) Evaluation of physicochemical mechanical and biological properties of chitosan/carboxymethyl cellulose reinforced with multiphasic calcium phosphate whisker-like fibers for bone tissue engineering. Mat Sci Eng: C 100:341-353. https://doi.org/10.1016/j.msec.2019.03.015

Mittal H, Ray SS, Kaith BS, Bhatia JK, Sharma J, Alhassan SM (2018) Recent progress in the structural modification of chitosan for applications in diversified biomedical fields. Eur Polym J 109:402–434. https://doi.org/10.1016/j.eurpolymj.2018.10.013

Miyaji F, Kono Y, Suyama Y (2005) Formation and structure of zinc-substituted calcium hydroxyapatite. Mater Res Bull 40:209–220. https://doi.org/10.1016/j.materresbull.2004.10.020

Pu X-m, Wei K, Zhang Q-q (2013) In situ forming chitosan/hydroxyapatite rods reinforced via genipin crosslinking. Mat Lett 94:169–171. https://doi.org/10.1016/j.matlet.2012.12.009

Raland RD, Borah JP (2016) Efficacy of heat generation in CTAB coated Mn doped ZnFe2O4 nanoparticles for magnetic hyperthermia. J Phys d: Appl Phys 50(3):035001. https://doi.org/10.1088/1361-6463/aa4e9a/meta

Rogina A, Rico P, Gallego Ferrer G, Ivanković M, Ivanković H (2016) n situ hydroxyapatite content affects the cell differentiation on porous chitosan/hydroxyapatite scaffolds. Annals Biomed Eng 44(4):1107–1119. https://doi.org/10.1007/s10439-015-1418-0

Sadeghinia A, Soltani S, Aghazadeh M, Khalilifard J, Davaran S (2020) Design and fabrication of clinoptilolite–nanohydroxyapatite/chitosan–gelatin composite scaffold and evaluation of its effects on bone tissue engineering. J Biomed Mat Res Part A 108(2):221-233. https://doi.org/10.1002/jbm.a.36806

Sainitya R, Sriram M, Kalyanaraman V, Dhivya S, Saravanan S, Vairamani M, Sastry TP, Selvamurugan N (2015) Scaffolds containing chitosan/carboxymethyl cellulose/mesoporous wollastonite for bone tissue engineering. Int J Biol Macromol 80:481-488. https://doi.org/10.1016/j.ijbiomac.2015.07.016

Samani S, Hossainalipour SM, Tamizifar M, Rezaie HR (2013) In vitro antibacterial evaluation of sol–gel-derived Zn-, Ag-, and (Zn+ Ag)-doped hydroxyapatite coatings against methicillin-resistant Staphylococcus aureus. J Biomed Mater Res Part A 101(1):222–230. https://doi.org/10.1002/jbm.a.34322

Saxena V, Shukla I, Pandey LM (2019) Chapter 8 - Hydroxyapatite: an inorganic ceramic for biomedical applications. In: Holban A-M, Grumezescu AM Materials for Biomedical Engineering 205–249. https://doi.org/10.1016/B978-0-12-816909-4.00008-7

Saxena V, Chandra P, Pandey LM (2018a) Design and characterization of novel Al-doped ZnO nanoassembly as an effective nanoantibiotic applied. Nanoscience 8:1925–1941. https://doi.org/10.1007/s13204-018-0863-0

Saxena V, Hasan A, Pandey LM (2018b) Effect of Zn/ZnO integration with hydroxyapatite: A review. Mater Technol 33:79–92. https://doi.org/10.1080/10667857.2017.1377972

Saxena V, Pandey LM (2020) Bimetallic assembly of Fe (III) doped ZnO as an effective nanoantibiotic and its ROS independent antibacterial mechanism. J Trace Elem Med Biol Organ Soc Min Trace Elem (GMS) 57:126416. https://doi.org/10.1016/j.jtemb.2019.126416

Schoolaert E, Cossu L, Becelaere J, Van Guyse JFR, Tigrine A, Vergaelen M, Hoogenboom R, De Clerck K (2020) Nanofibers with a tunable wettability by electrospinning and physical crosslinking of poly(2-n-propyl-2-oxazoline). Mat Design 192108747. https://doi.org/10.1016/j.matdes.2020.108747

Shavandi A, Bekhit AE-DA, Ali MA, Sun Z, Gould M (2015) Development and characterization of hydroxyapatite/β-TCP/chitosan composites for tissue engineering applications. Mat Sci Eng: C 56:481–493. https://doi.org/10.1016/j.msec.2015.07.004

Shen L, Yang H, Ying J, Qiao F, Peng M (2009) Preparation and mechanical properties of carbon fiber reinforced hydroxyapatite/polylactide biocomposites. J Mater Sci Mater Med 20:2259–2265. https://doi.org/10.1007/s10856-009-3785-2

Sivashankari PR, Prabaharan M (2020) Three-dimensional porous scaffolds based on agarose/chitosan/graphene oxide composite for tissue engineering. Int J Biol Macromol 146:222-231. https://doi.org/10.1016/j.ijbiomac.2019.12.219

Spath S, Drescher P, Seitz HJM (2015) Impact of particle size of ceramic granule blends on mechanical strength and porosity of 3D printed scaffolds Mater 8:4720–4732. https://doi.org/10.3390/ma8084720

Srilakshmi C, Saraf R (2016) Ag-doped hydroxyapatite as efficient adsorbent for removal of Congo red dye from aqueous solution: Synthesis, kinetic and equilibrium adsorption isotherm analysis Microporous Mesoporous Mater 219:134–144. https://doi.org/10.1016/j.micromeso.2015.08.003

Sun X, Mei C, French AD, Lee S, Wang Y, Wu Q (2018) Surface wetting behavior of nanocellulose-based composite films. Cellulose 25:5071–5087. https://doi.org/10.1007/s10570-018-1927-8

Šupová M (2015) Substituted hydroxyapatites for biomedical applications: A review. Ceram Int 41:9203–9231. https://doi.org/10.1016/j.ceramint.2015.03.316

Venkatesan J, Pallela R, Bhatnagar I, Kim SK (2012) Chitosan–amylopectin/hydroxyapatite and chitosan–chondroitin sulphate/hydroxyapatite composite scaffolds for bone tissue engineering. Int J Biol Macromol 51(5):1033–1042. https://doi.org/10.1016/j.ijbiomac.2012.08.020

Vilela PB, Dalalibera A, Duminelli EC, Becegato VA, Paulino AT (2019) Adsorption and removal of chromium (VI) contained in aqueous solutions using a chitosan-based hydrogel. Environmental Science and Pollution Research 26(28):28481–28489. https://doi.org/10.1007/s11356-018-3208-3

Wahlström N, Edlund U, Pavia H, Toth G, Jaworski A, Pell AJ, Richter-Dahlfors A (2020) Cellulose from the green macroalgae Ulva lactuca: isolation, characterization, optotracing, and production of cellulose nanofibrils. Cellulose 27(7):3707–3725. https://doi.org/10.1007/s10570-020-03029-5

Wallecan J, Debon SJJ (2018) Strong cationic polyelectrolyte adsorption on a water swollen cellulosic biomaterial and its relevance on microstructure and rheological properties. Cellulose 25:4437–4451. https://doi.org/10.1007/s10570-018-1887-z

Wang B, Huang C, Chen S, Xing X, Zhang M, Wu Q, Wang H (2018) Hybrid scaffolds enhanced by nanofibers improve in vitro cell behavior for tissue regeneration. Cellulose 25:7113–7125. https://doi.org/10.1007/s10570-018-2087-6

Wang Y, Liu L, Guo S (2010) Characterization of biodegradable and cytocompatible nano-hydroxyapatite/polycaprolactone porous scaffolds in degradation in vitro. Polym Degrad Stabil 95(2):207–213. https://doi.org/10.1016/j.polymdegradstab.2009.11.023

Wang F, Pang Y, Chen Weiwei, Wang Zhongmin, Chen (2020) Enhanced physical and biological properties of chitosan scaffold by silk proteins cross-linking. Carbohydrate Polymers 229115529. https://doi.org/10.1016/j.carbpol.2019.115529

Xiu ZM, Zhang QB, Puppala HL, Colvin VL, Alvarez PJ (2012) Negligible particle-specific antibacterial activity of silver

nanoparticles. Nano Lett 12(8):4271–4275. https://doi.org/10.1021/nl301934w

Zhao Y, Sun B, Wang T, Yang L, Xu X, Chen C, Sun D (2020) Synthesis of cellulose–silica nanocomposites by in situ biomineralization during fermentation. Cellulose 27(2):703–712. https://doi.org/10.1007/s10570-019-02824-z